PET Imaging of Macrophage Mannose Receptor–Expressing Macrophages in Tumor Stroma Using ^{18}F-Radiolabeled Camelid Single-Domain Antibody Fragments

Anneleen Blykers*[1], Steve Schoonooghe*[2,3], Catarina Xavier*[1], Kevin D'hoe[2,3], Damya Laoui[2,3], Matthias D'Huyvetter[1], Ilse Vaneycken[1,4], Frederik Cleeren[5], Guy Bormans[5], Johannes Heemskerk[1,4], Geert Raes[2,3], Patrick De Baetselier[2,3], Tony Lahoutte[1,4], Nick Devoogdt[1,2], Jo A. Van Ginderachter*[2,3], and Vicky Caveliers*[1,4]

[1]In Vivo Cellular and Molecular Imaging laboratory (ICMI), Vrije Universiteit Brussel, Brussels, Belgium; [2]Laboratory of Cellular and Molecular Immunology (CMIM), Vrije Universiteit Brussel, Brussels, Belgium; [3]Laboratory of Myeloid Cell Immunology (MCI), VIB, Brussels, Belgium; [4]Department of Nuclear Medicine, UZ Brussel, Brussels, Belgium; and [5]Laboratory for Radiopharmacy, KU Leuven, Leuven, Belgium

Tumor-associated macrophages constitute a major component of the stroma of solid tumors, encompassing distinct subpopulations with different characteristics and functions. We aimed to identify M2-oriented tumor-supporting macrophages within the tumor microenvironment as indicators of cancer progression and prognosis, using PET imaging. This can be realized by designing ^{18}F-labeled camelid single-domain antibody fragments (sdAbs) specifically targeting the macrophage mannose receptor (MMR), which has been identified as an important biomarker on this cell population. **Methods:** Cross-reactive anti-MMR sdAbs were generated after immunization of an alpaca with the extracellular domains of both human and mouse MMR. The lead binder was chosen on the basis of comparisons of binding affinity and in vivo pharmacokinetics. The PET tracer ^{18}F-fluorobenzoate (FB)-anti-MMR sdAb was developed using the prosthetic group N-succinimidyl-4-^{18}F-fluorobenzoate (^{18}F-SFB), and its biodistribution, tumor-targeting potential, and specificity in terms of macrophage and MMR targeting were evaluated in mouse tumor models. **Results:** Four sdAbs were selected after affinity screening, but only 2 were found to be cross-reactive for human and mouse MMR. The lead anti-MMR 3.49 sdAb, bearing an affinity of 12 and 1.8 nM for mouse and human MMR, respectively, was chosen for its favorable in vivo biodistribution profile and tumor-targeting capacity. ^{18}F-FB-anti-MMR 3.49 sdAb was synthesized with a 5%–10% radiochemical yield using an automated and optimized protocol. In vivo biodistribution analyses showed fast clearance via the kidneys and retention in MMR-expressing organs and tumor. The kidney retention of the fluorinated sdAb was 20-fold lower than a ^{99m}Tc-labeled counterpart. Compared with MMR- and C-C chemokine receptor 2–deficient mice, significantly higher uptake was observed in tumors grown in wild-type mice, demonstrating the specificity of the ^{18}F tracer for MMR and macrophages, respectively. **Conclusion:** Anti-MMR 3.49 was denoted as the lead cross-reactive MMR-targeting sdAb. [18]F radiosynthesis was optimized, providing an optimal probe for PET imaging of the tumor-promoting macrophage subpopulation in the tumor stroma.

During tumor development, myeloid cells are attracted to the tumor stroma. These infiltrating immune cells are versatile, adopting different activation states in response to a changing microenvironment, leading to subsets of tumor-associated macrophages (TAMs) with specialized functions (1,2). Two main morphologically distinct TAM subsets can be distinguished on the basis of major histocompatibility complex (MHC) class II expression levels in multiple mouse tumor models. Tumor promotion has been linked with an accumulation of M2-oriented MHC II[low] TAMs in lung and breast carcinoma (3,4). Accordingly, MHC II[low] TAMs were found to reside primarily in less oxygenated zones, express hypoxia-regulated genes, and facilitate the angiogenic switch (5). Interestingly, the macrophage mannose receptor (MMR, CD206), a typical M2 cell surface marker, is upregulated on these tumor-promoting MHC II[low] TAMs in all tumor models studied (3–5). The M1/M2 nomenclature has shortcomings, and a better positioning of TAM subsets within the spectrum of macrophage activation states is warranted (6).

Overall, it is becoming clear that a more detailed insight into the molecular and functional characteristics of the tumor stromal cells is crucial for a better understanding of cancer progression and response to treatment. This is also reflected in the fact that therapies are being developed aiming specifically at the stromal compartment or tumor-infiltrating immune cells. Together with these new therapies, targeted imaging probes are needed. The potential of radiolabeled camelid single-domain antibody fragments (sdAbs; VHH, Nanobodies [Nanobody is a trade name of Ablynx NV]) for imaging of macrophages and dendritic cells has been demonstrated (7–9). ^{99m}Tc-labeled sdAbs specifically targeting murine MMR were found to be interesting new probes for preclinical imaging of MHC II[low] TAMs within the tumor microenvironment (10).

To validate anti-MMR sdAbs as imaging tools for ultimate clinical translation, new cross-reactive antimouse/human MMR

sdAbs were generated. They enable clinical applications after preclinical validation in appropriate mouse models (11). ^{18}F is an attractive PET isotope with a 110-min half-life and low-energy positron (maximally 0.635 MeV) emitted. In addition, an in-house cyclotron allows starting with high initial activities and distribution of ^{18}F-labeled compound between centers. Direct ^{18}F fluorination methods of proteins are not suited because harsh reaction conditions such as high reaction temperatures and dipolar aprotic solvents are usually needed. Alternatively, radio-fluorination can be achieved through the use of small ^{18}F-labeled reactive precursors that act as a prosthetic tag to the biomolecule (12). N-succinimidyl-4-^{18}F-fluorobenzoate (^{18}F-SFB) is the most common prosthetic group used as synthon for protein labeling with ^{18}F (12–14).

Here, we describe the generation and selection of a lead cross-reactive anti-MMR sdAb, optimization of the ^{18}F radiochemistry, and validation of the PET probe in mouse tumor models.

MATERIALS AND METHODS

sdAb Generation and Selection of Lead Compound

Anti-MMR sdAbs were isolated from an immune sdAb phage-display library after immunization of an alpaca (*Vicugna pacos*) according to a 6-wk alternating schedule of weekly injections of recombinant human or mouse monomeric fusion proteins ($11,15$). After production of sdAb-displaying bacteriophages in *Escherichia coli*, biopannings and enzyme-linked immunosorbent assay screenings were performed to select MMR binding sdAbs. Purification of the hexahistidine-tagged sdAbs from the periplasm was performed as described previously ($11,15$). The binding characteristics of selected sdAbs were compared using surface plasmon resonance and flow cytometry. The detailed procedure is described in the supplemental materials (available at http://jnm.snmjournals.org). BcII10, an irrelevant sdAb binding to a bacterial enzyme, was used as a nontargeting control Nanobody (16). Anti-MMR sdAbs were radiolabeled using ^{99m}Tc-tricarbonyl chemistry as previously described to compare the in vivo biodistribution profile and select a lead compound (17–19). In vitro specificity was established as described in the supplemental materials.

^{18}F Labeling of Lead sdAb

^{18}F-SFB Synthesis. Cyclotron-produced ^{18}F-fluoride was separated from ^{18}O-enriched water on a SepPak light accell plus QMA anion exchange cartridge (Waters) and eluted using 600 μL of a solution containing 4.2 mg of K_2CO_3 and 22.6 mg of Cryptand (K_{222}) in acetonitrile/water (1:1) (ABX). The solvent was evaporated to generate the anhydrous $K_{222}/K[^{18}F]F$ complex.

The ^{18}F-SFB prosthetic group was synthesized using disposable cassettes (IFP Nucleophilic) on a Synthera module (IBA Molecular) in a 3-step, 1-pot reaction. A solution of 4 mg (0.011 mmol) of ethyl 4-(trimethylammonium)benzoate (ABX) in 2 mL of dimethylsulfoxide (Sigma-Aldrich) was added to the dried ^{18}F-F$^-$ complex in the reaction vial and heated to 110°C for 15 min to produce ethyl-4-^{18}F-fluorobenzoate. This compound was hydrolyzed at 95°C for 5 min by adding 20 μL (0.02 mol) of a 0.1 M tetrapropylammoniumhydroxide solution. Subsequent activation was performed with 26 mg (0.072 mmol) of N,N,N′,N′-tetramethyl-O-(N-succinimidyl) uronium hexafluorophosphate in 1 mL of acetonitrile (CH$_3$CN) at 110°C for 5 min to form ^{18}F-SFB. The reaction mixture was remotely transferred to a second Synthera, diluted with 4 mL of 4.8% acetic acid solution/8 mL of 0.9% NaCl and purified on a solid-phase extraction cartridge (SPE). The cartridge was washed with 20% aqueous CH$_3$CN (5 mL) and eluted with CH$_3$CN

(2.5 mL). The purification was optimized using either a C18 plus short (Waters) or an AFFINIMIP (Polyintell) SPE cartridge. The purified ^{18}F-SFB was transferred to a conical vial, placed in a home-made semi-automatic module connected to the Synthera box, and evaporated to dryness by means of gentle heating and nitrogen stream.

^{18}F-Fluorobenzoate (FB)-Anti-MMR sdAb Synthesis. Conjugation conditions of the sdAb to ^{18}F-SFB were optimized in terms of temperature, protein concentration, incubation time, and pH. A solution of sdAb (50–250 μg, 3.7–18.5 nmol) in 300 μL of borate buffer (0.1 M, pH 7.4–9.0) was prepared and added to the dried ^{18}F-SFB (1.0–7.5 GBq) reaction vial. After incubation, the mixture was purified by size-exclusion chromatography using a PD-10 column (GE Healthcare) and passed through a 0.22-μm filter (Millipore).

Radiochemical identity and purity were assessed by reversed-phase high-performance liquid chromatography (RP-HPLC) using a Hitachi Chromaster system (VWR) connected to a diode array and γ detector (Raytest). The identity of the main compound was confirmed using unlabeled sdAb as reference material. A polystyrene divinylbenzene copolymer column (PLRP-S 300 Å, 5 μm, 250/4 mm; Agilent) was used with the following gradient applied (A: 0.1% trifluoroacetic acid in water; B: 0.1% trifluoroacetic acid in acetonitrile): 0–5 min 25% B; 5–7 min 25%–34% B; 7–10 min 34%–100% B; 10–25 min 100% B at a flow rate of 1 mL min^{-1} (retention time: ^{18}F-FB-anti-MMR sdAb, 12.5 min; ^{18}F$^-$, 3–4 min; ^{18}F-SFB, 13.5 min).

Animal Models

Wild-type (WT) C57BL/6 mice (Janvier) were used for in vivo stability studies. To evaluate biodistribution and targeting specificity, C57BL/6 WT, MMR-deficient (MMR knock-out [KO]), and C-C chemokine receptor type 2–deficient (CCR2-KO) mice were subcutaneously inoculated in the right flank with 3×10^6 of the 3LL-R clone of Lewis lung carcinoma cells suspended in Hank's balanced salt solution medium. Tumors were allowed to grow for 12 d (750–1,000 mm^3). The local ethics committee for animal research has approved the study protocol.

Biodistribution Studies and PET/CT Imaging

3LL-R tumor–bearing mice, anesthetized with 2.5% isoflurane, were injected intravenously with ^{99m}Tc-anti-MMR sdAb (30–70 MBq, 5 μg of sdAb) or ^{18}F-FB-anti-MMR sdAb (3.2–4.0 MBq, 5 μg of sdAb) via the tail. Mice were sacrificed at 3 h after injection, and major organs were collected, weighed, and counted against a standard of known activity in a γ counter. Tissue/organ uptake was calculated and expressed as a percentage injected activity per gram (%IA/g), corrected for decay. From a separate group of animals, blood samples were collected 1, 5, 10, 20, 40, 60, and 120 min after ^{18}F-FB-anti-MMR sdAb injection, via a microcapillary, and analyzed in the γ counter to obtain a blood time–activity curve. The half-life was calculated using a biexponential nonlinear regression fit (GraphPad Prism; GraphPad Software). Furthermore, urine samples of 3 mice were collected after 30 min and injected on RP-HPLC to detect radiometabolites.

Small-animal PET was performed on a Focus 220 microPET scanner (Concorde Microsystems). Mice were injected with 8.8–9.3 MBq of the tracer via the tail vein, and after 60 and 180 min, static PET scans were acquired together with micro-CT scans to provide anatomic information and attenuation correction of the PET signal. During all scanning sessions, animals were kept under gas anesthesia (2.5% isoflurane). High-resolution images were reconstructed using filtered backprojection and maximum a posteriori for small-animal PET and micro-CT, respectively. Image viewing was performed with AMIDE imaging software. Regions of interest were drawn over the tumor to evaluate tracer accumulation.

Autoradiography

Dissected tumors were freshly frozen using O.C.T. solution (VWR). Tumor sections (5–10 μm) were obtained using a cryotome (Shandon cryotome FSE; Thermo Fisher), mounted on adhesive microscope slides (Superfrost Plus; Thermo Fisher), and exposed to a phosphor storage screen film (Perkin Elmer) for about 12 h. The screens were read using a Cyclone Plus system (Perkin Elmer) and analyzed using Optiquant software (Perkin Elmer).

Statistical Analysis

Quantitative data are expressed as mean ± SD and compared using the independent t test after proving normal distribution via the Shapiro–Wilk test using SPSS Statistics (IBM Corp.).

RESULTS

Antihuman/Mouse MMR sdAb Generation and Selection of Lead Compound

sdAbs were generated against the recombinant extracellular domains of human and mouse MMR. Enzyme-linked immunosorbent assay screenings and sequencing of individual clones led to the identification of 27 clonally unrelated sdAb families. From these, 17 families appeared to be cross-reactive with human MMR and mouse MMR. Surface plasmon resonance measurements of 30 different sdAbs, out of these families, revealed several binders with nanomolar affinity. On the basis of the observed affinities and diversity in CDR3 regions, 4 potentially cross-reactive clones (14.4, 5.38, 26.7, and 3.49; Table 1) were selected for a more in-depth in vitro characterization. Among them, only 14.4 and 3.49 showed affinity for both human and mouse MMR-expressing cells in flow cytometry (Fig. 1), suggesting that only these sdAbs recognize both the recombinant and the native versions of MMR. Subsequently, anti-MMR 3.49 and 14.4 were labeled with ^{99m}Tc, and a biodistribution study in 3LL-R tumor–bearing mice showed fast renal clearance in addition to specific retention in the liver, spleen, lymph nodes, bone, and tumor (Table 2). Superior features in comparison with ^{99m}Tc-anti-MMR 14.4, including higher tumor and lower spleen and liver uptake, designated anti-MMR 3.49 sdAb as the lead compound. The binding specificity of ^{99m}Tc-anti-MMR 3.49 was assessed by an in vitro blocking study on recombinant MMR (Supplemental Fig. 1), and importantly target specificity was also confirmed in vivo because no tracer uptake was observed in MMR-deficient mice, except for the normal excretion route (Table 2).
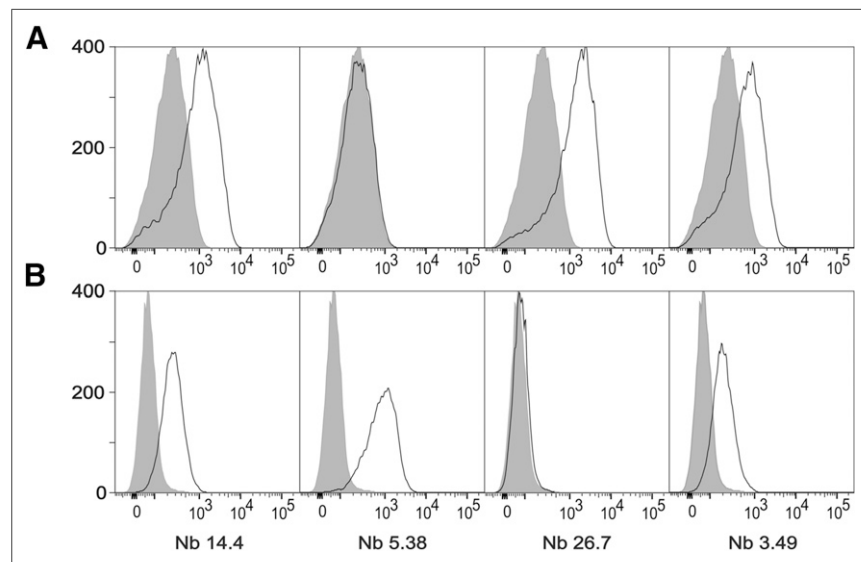
^{18}F Labeling of Lead sdAb

Radiofluorination of anti-MMR 3.49 sdAb was accomplished by conjugation of the antibody fragment to the prosthetic group ^{18}F-SFB. ^{18}F-SFB was synthesized on a Synthera module in a 3-step, 1-pot reaction. Synthesis and purification resulted in a radiochemical yield of 50%–60% in 90 min, with a radiochemical purity greater than 95%. For subsequent conjugation, the addition of sdAb (1 mg/mL) in 0.1 M borate buffer, pH 8.4–8.5, and incubation for 20 min at room temperature resulted in the generation of ^{18}F-FB-anti-MMR 3.49 with a 20%–30% decay-corrected conjugation yield. A pH below 8.5 (pH 7.4–8.3) lowered the reactivity of the sdAbs' amino groups toward acylation, whereas a pH above 8.5 (pH 8.6–9.0) induced degradation of ^{18}F-SFB, decreasing the coupling yield in both cases to 5%–15% (decay-corrected) as shown in Supplemental Table 1. This

FIGURE 1. (A) Staining of single-cell suspensions prepared from 15-d-old 3LL-R subcutaneous tumors grown in C57BL/6 WT mice. (B) Staining on immature human dendritic cells expressing human MMR. Shaded histograms represent sdAb BCII10–negative control staining.

TABLE 2
Biodistribution of 99mTc-Anti-MMR sdAbs in 3LL-R–Bearing WT and MMR-KO Mice

Organ/tissue	99mTc-anti-MMR 3.49 WT (n = 3)	99mTc-anti-MMR 14.4 WT (n = 3)	99mTc-anti-MMR 3.49 MMR-KO (n = 2)
Heart	2.18 ± 0.15	2.77 ± 0.77	0.14 ± 0.02
Lungs	1.44 ± 0.15	0.92 ± 0.28	0.40 ± 0.08
Liver	14.79 ± 0.52	27.37 ± 3.37	0.61 ± 0.05
Spleen	4.94 ± 0.32	6.20 ± 1.69	0.22 ± 0.04
Kidney	146.61 ± 2.85	69.30 ± 11.46	234.77 ± 25.91
Muscle	0.57 ± 0.14	0.42 ± 0.11	0.06 ± 0.02
Bone	1.88 ± 0.17	1.78 ± 0.81	0.12 ± 0.01
Lymph nodes	3.04 ± 0.33	3.02 ± 0.46	0.19 ± 0.04
Blood	0.30 ± 0.03	0.13 ± 0.02	0.18 ± 0.03
Tumor	2.41 ± 0.34	1.40 ± 0.26	Not done

Data were obtained at 3 h after injection and expressed as mean %IA/g ± SD.

accelerated ^{18}F-SFB degradation was also observed after longer reaction times. A radiochemical purity of greater than 97% (Fig. 2) and a global yield of 5%–15% (decay-corrected, starting from ^{18}F-F^{-}) in 180 min were obtained. Furthermore, the tracer was stable in phosphate-buffered saline, pH 7.4, for at least 3 h (Fig. 2). The specific activity ranged from 10 to 30 GBq/μmol.

In Vivo Biodistribution and Tumor Targeting of ^{18}F-FB-Anti-MMR sdAb

^{18}F-FB-anti-MMR 3.49 injection in 3LL-R tumor–bearing mice showed specific retention in MMR-expressing organs/tissues, in-

FIGURE 2. RP-HPLC analysis of purified ^{18}F-FB-anti-MMR 3.49 sdAb (A; γ trace black, left axis; UV trace blue, right axis; retention time = 12.5 min) and after incubation for 3 h in phosphate-buffered saline, pH 7.4, at room temperature (B; γ trace). (C) Reversed-phase chromatogram of urine obtained 30 min after injection of ^{18}F-FB-anti-MMR 3.49 (γ trace).

cluding tumor (2.40 ± 0.46 %IA/g), whereas negligible uptake was observed in MMR-deficient hosts (Table 3). Importantly, tumor uptake of the tracer in CCR2-deficient mice, which contain strongly reduced macrophage numbers in the tumor microenvironment, was significantly lower ($P < 0.05$) than the tumor uptake in WT mice (Table 3), confirming the in vivo recognition of TAMs. The low bone uptake indicated that no in vivo defluorination occurred. Remarkably, kidney uptake of ^{18}F-sdAb 3 h after tracer injection (Table 3) was about 20-fold lower than with the ^{99m}Tc-labeled sdAb in the same tumor model (Table 2). Furthermore, a significant decrease in extratumoral uptake in the liver and spleen was also observed (Fig. 3).

The blood time–activity curve confirmed rapid clearance of ^{18}F-sdAb from the blood, after a biphasic profile (Supplemental Fig. 2) with half-lives of 1.4 and 39.1 min. RP-HPLC analysis of urine samples obtained from naive mice injected with ^{18}F-FB-anti-MMR 3.49 sdAb confirmed metabolization (Fig. 2), which enhanced the elimination of activity from the kidneys.

PET images were in line with the ex vivo biodistribution data. The highest signal was present in the bladder, confirming renal clearance. Furthermore, specific retention in the tumor (Fig. 4) and MMR-expressing tissue such as the liver (Supplemental Fig. 3) was observed. In MMR-deficient mice, the tracer was excreted without uptake in tissues or organs except for the kidneys and bladder, strengthening the target specificity of the tracer. A 3-times-higher mean uptake in tumors grown in WT mice, compared with tumors grown in MMR-deficient mice, was measured. Intratumoral tracer distribution, using ex vivo autoradiography (Fig. 4), showed a nonhomogeneous pattern, with higher uptake at the border and some focal hotspots.

DISCUSSION

Immune cells, and especially macrophages, present in the tumor stroma contribute to cancer development (1–4). The MMR receptor (CD206) was identified as a marker for M2-oriented MHC II^{low} TAMs, which were shown to be strongly angiogenic and immunosuppressive, suggestive of a tumor-promoting role in vivo (3). Accordingly, the presence of M2-oriented macrophages significantly
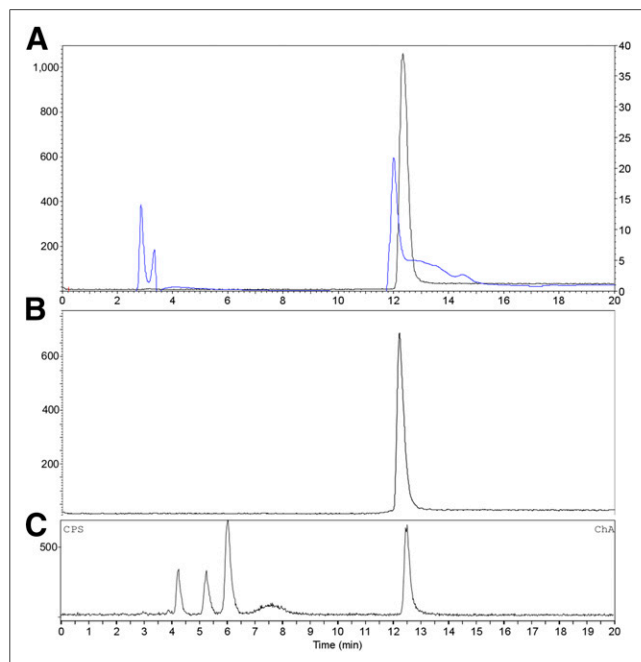
TABLE 3
Biodistribution of ^{18}F-FB-Anti-MMR 3.49 sdAb in 3LL-R–Bearing WT, MMR-Deficient, and CCR-2–Deficient Mice at 3 Hours After Injection

Organ/tissue	WT mice (n = 8)	MMR-KO mice (n = 8)	CCR2-KO mice (n = 5)
Lungs	1.60 ± 0.40	0.82 ± 0.52	1.45 ± 0.14
Heart	0.81 ± 0.11	0.28 ± 0.12*	1.00 ± 0.14
Liver	2.26 ± 0.51	0.52 ± 0.30*	2.54 ± 0.31
Spleen	1.34 ± 0.31	0.38 ± 0.16*	1.71 ± 0.69
Kidney	7.98 ± 0.86	4.76 ± 2.76	7.60 ± 0.76
Muscle	0.37 ± 0.14	0.10 ± 0.07*	0.42 ± 0.27
Bone	0.67 ± 0.28	0.15 ± 0.02*	1.03 ± 0.20
Blood	1.02 ± 0.31	0.73 ± 0.31	1.16 ± 0.20
Tumor	2.40 ± 0.46	0.29 ± 0.14*	1.42 ± 0.17†

*Data are significantly different, $P < 0.05$.
Data are expressed as mean %IA/g ± SD.

correlates with a worse prognosis in multiple tumor types (20,21). Moreover, MHC II[low] TAMs are predominantly present in hypoxic zones of the tumor stroma, albeit that the lower oxygen tension is not the major driver of the polarization into a MHC II[low] MMR[hi] phenotype (5). This suggests a scenario in which macrophages are skewed toward an MHC II[hi]/MMR[low] or an MHC II[low]/MMR[hi] phenotype under the influence of microenvironmental cues other than hypoxia, with the latter population preferentially migrating to hypoxic tumor areas. Given this knowledge, noninvasive imaging of MMR[hi] TAM could be of prognostic value and might aid in the visualization of hypoxic tumor areas.

sdAbs (10–15 kDa) can be used for molecular imaging after their efficient tumor penetration in combination with rapid tracer elimination from circulation, enabling imaging at early time points. MMR-specific cross-reactive sdAbs that recognize both the mouse and the human target biomarker were generated to trace MMR^{hi} cells in animal tumor models with a clear prospect toward clinical translation (22). The path from sdAb generation after alpaca immunization to the selection of a lead candidate for MMR imaging involved several affinity screening assays and has identified anti-MMR 3.49 sdAb for the development of ^{18}F radiochemistry and further in vivo characterization. Compared with SPECT, PET may improve the imaging of the tumor stroma because of its inherently higher sensitivity and substantially better and more uniform spatial resolution. The synthesis of ^{18}F-SFB was successfully automated on Synthera after a 3-step, 1-pot synthesis. In comparison with Ackermann et al. (23), our optimized synthesis protocol required a larger reaction volume for fluorination and no drying step after basic hydrolysis. The use of more than 4 mg of precursor resulted in more impurities with minor increase of labeling yield. As such, after optimization of the reaction steps, a reliable synthesis was obtained in 50 min with a 60%–70% decay-corrected yield. Instead of using 3 purification cartridges, 1 cartridge was sufficient to remove impurities as reported by Thonon et al. (13). A conventional C18 cartridge was compared with a molecularly imprinted cartridge. Although the chemical purity was higher using AFFINIMIP (no excess of pre-

cursor identified using mass spectrometry, data not shown), radiochemical purity after C18 purification stayed above 95%, enabling the use of both.

Comparable or lower conjugation yields are described when coupling ^{18}F-SFB to diabodies resulting in conjugation yields of 5%–15% (24,25). Nevertheless, dissolving ^{18}F-SFB in organic solvent omitted its low stability in aqueous conditions and improved conjugation yields (26–29). Moreover, these conjugation yields exceeding 20% are achievable only when highly concentrated protein or peptide solutions are provided, in agreement with the conclusion of Wuest et al. (30). One milligram of sdAb solution per milliliter, in our case, provided acceptable yields exceeding 20%. The automated protocol enabled the production of ^{18}F-FB-anti-MMR sdAb with sufficient activity to perform a clinical study (200–500 MBq).

^{18}F-FB-anti-MMR sdAb specifically recognized MMR in 3LL-R–bearing mice when compared with tracer uptake in the MMR-deficient tumor recipients and was rapidly cleared from the circulation, as evidenced by both small-animal PET imaging and biodistribution studies. In addition, CCR2-deficient mice were used to assess the recognition of macrophages. These mice have strongly reduced monocyte numbers in their circulation, leading to much lower levels of monocyte-derived macrophages in inflammatory sites such as tumors, including 3LL-R tumors (3). Decreased tumor uptake in CCR2-deficient animals supports targeting of stromal macrophages.

Importantly, the degree of kidney retention of fluorinated sdAb is 20-fold lower than its [99mTc] analog at the 3-h time point. Renal catabolism probably produced hydrophobic or nonresidualizing metabolites, which diffuse out of the tubular cells and are in this way more easily cleared from the body (31,32). This hypothesis was supported by the identification of radiometabolites in urine. In contrast, radiometal-labeled counterparts have the tendency to be retained in kidneys (32). Moreover, the fluorinated tracer showed decreased binding to extratumoral sites, while preserving tumor targeting. Although speculative, this decreased binding to extratumoral sites could be attributed to distinct physiologic properties of [99mTc]- and ^{18}F-labeled probes: different specific activities, charge, processing of the probe after receptor binding in liver and spleen (the MMR-positive organs that are mostly affected by the differential labeling strategies), and metabolization (25). The different specific activities of the radiolabeled sdAbs result in various ratios of labeled to nonlabeled sdAb injected, and the latter could contribute to the binding to and blocking of available receptors depending on blood flow and vascular permeability in the concerning tissue.
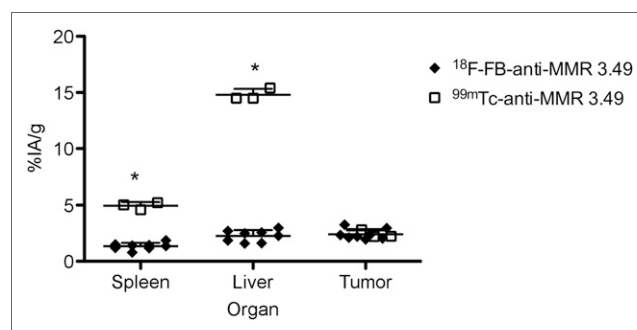

FIGURE 3. Comparison between uptake of ^{18}F-FB-anti-MMR 3.49 sdAb (♦) and [99mTc]-anti-MMR 3.49 sdAb (□) in spleen, liver, and tumor 3 h after injection. *Data are significantly different, $P < 0.05$.
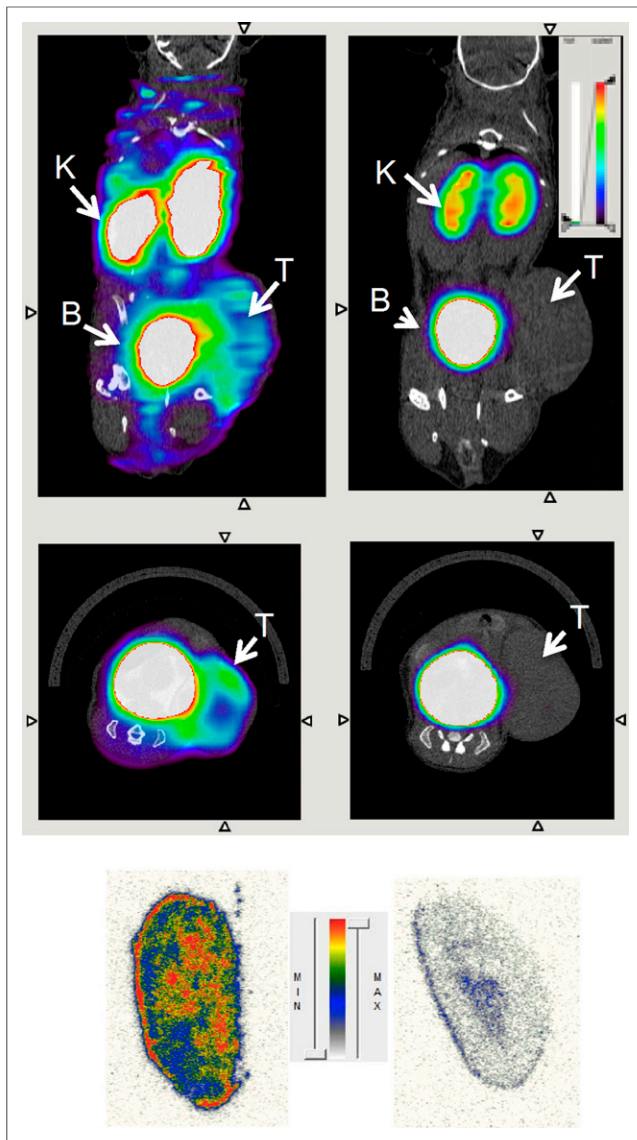
FIGURE 4. Transverse and coronal PET/CT images of WT (left) vs. MMR-deficient (right) 3LL-R tumor–bearing mice scanned 3 h after injection of ^{18}F-FB-anti MMR 3.49. PET signals are encoded in color scale, CT image in gray scale. Arrows point to tumor (T), kidney (K), and bladder (B). Autoradiography performed on slices from 3LL-R tumors grown in WT (left) vs. MMR-deficient (right) mice. max = maximum; min = minimum.

The preclinical in vivo results show a high potential for clinical implementation because the combination of the ^{18}F label (PET) with the specificity and affinity of camelid sdAbs is promising. Because the presence of MMR[hi] M2-like TAMs correlates with malignant progression, this probe could have significant added value in staging solid tumors and as a prognostic tool.

CONCLUSION

Cross-reactive anti-MMR sdAbs were produced and screened. Anti-MMR 3.49 sdAb was selected as the most potent candidate for the development of a new PET radiopharmaceutical. An efficient and reproducible ^{18}F-labeling approach was developed, and the biologic behavior of the tracer toward macrophage and

MMR targeting was investigated. ^{18}F-FB-anti-MMR sdAb is a favorable new PET probe for detecting MMR-expressing TAMs, providing prognostic information about the tumor stroma.

REFERENCES

1. Lewis CE, Pollard JW. Distinct role of macrophages in different tumor microenvironments. *Cancer Res.* 2006;66:605–612.
2. Allavena P, Sica A, Solinas G, Chiara Porta C, Mantovani A. The inflammatory microenvironment in tumor progression: the role of tumor-associated macrophages. *Crit Rev Oncol Hematol.* 2008;66:1–9.
3. Movahedi K, Laoui D, Gysemans C, et al. Different tumor microenvironments contain functionally distinct subsets of macrophages derived from Ly6C(high) Monocytes. *Cancer Res.* 2010;70:5728–5739.
4. Laoui D, Van Overmeire E, Movahedi K, et al. Mononuclear phagocyte heterogeneity in cancer: different subsets and activation states reaching out at the tumor site. *Immunobiology.* 2011;216:1192–1202.
5. Laoui D, Van Overmeire E, Di Conza G, et al. Tumor hypoxia does not drive differentiation of tumor-associated macrophages but rather fine-tunes the M2-like macrophage population. *Cancer Res.* 2014;74:24–30.
6. Murray PJ, Allen JE, Biswas SK, et al. Macrophage activation and polarization: nomenclature and experimental guidelines. *Immunity.* 2014;41:14–20.
7. Hamers-Casterman C, Atarhouch T, Muyldermans S, et al. Naturally-occurring antibodies devoid of light-chains. *Nature.* 1993;363:446–448.
8. Schoonooghe S, Laoui D, Van Ginderachter JA, et al. Novel applications of nanobodies for in vivo bio-imaging of inflamed tissue in inflammatory disease and cancer. *Immunobiology.* 2012;217:1266–1272.
9. De Groeve K, Deschacht N, De Koninck C, et al. Nanobodies as tools for in vivo imaging of specific immune cell types. *J Nucl Med.* 2010;51:782–789.
10. Movahedi K, Schoonooghe S, Laoui D, et al. Nanobody-based targeting of the macrophage mannose receptor for effective in vivo imaging of tumor-associated macrophages. *Cancer Res.* 2012;72:4165–4177.
11. Broisat A, Hernot S, Toczek J, et al. Nanobodies targeting mouse/human VCAM1 for the nuclear imaging of atherosclerotic lesions. *Circ Res.* 2012;110:927–937.
12. Miller PW, Long NJ, Vilar R, Gee AD. Synthesis of ^{11}C, ^{18}F, ^{15}O, and ^{13}N radiolabels for positron emission tomography. *Angew Chem Int Ed Engl.* 2008;47:8998–9033.
13. Thonon D, Goblet D, Goukens E, et al. Fully automated preparation and conjugation of N-succinimidyl 4-[18F]fluorobenzoate ([18F]SFB) with RGD peptide using a GE FASTlab™ synthesizer. *Mol Imaging Biol.* 2011;13:1088–1095.
14. Tang G, Zeng W, Yu M, Kabalka G. Facile synthesis of N-succinimidyl 4-[18F] fluorobenzoate ([18F]SFB) for protein labeling. *J Labelled Comp Radiopharm.* 2008;51:68–71.
15. Vincke C, Gutiérrez C, Wernery U, Devoogdt N, Hassanzadeh-Ghassabeh G, Muyldermans S. Generation of single domain antibody fragments derived from camelids and generation of manifold constructs. *Methods Mol Biol.* 2012;907:145–176.
16. Conrath KE, Lauwereys M, Galleni M, et al. Beta-lactamase inhibitors derived from single-domain antibody fragments elicited in the camelidae. *Antimicrob Agents Chemother.* 2001;45:2807–2812.
17. Vaneycken I, Devoogdt N, Van Gassen N, et al. Preclinical screening of anti-HER2 nanobodies for molecular imaging of breast cancer. *FASEB J.* 2011;25:2433–2446.

18. Gainkam LO, Huang L, Caveliers V, et al. Comparison of the biodistribution and tumor targeting of two [99mTc]-labeled anti-EGFR nanobodies in mice, using pinhole SPECT/micro-CT. *J Nucl Med.* 2008;49:788–795.

19. Xavier C, Devoogdt N, Hernot S, et al. Site-specific labeling of his-tagged nanobodies with [99mTc]: a practical guide. *Methods Mol Biol.* 2012;911:485–490.

20. Galon J, Costes A, Sanchez-Cabo F, et al. Type, density, and location of immune cells within human colorectal tumors predict clinical outcome. *Science.* 2006;313:1960–1964.

21. Qian BZ, Pollard JW. Macrophage diversity enhances tumor progression and metastasis. *Cell.* 2010;141:39–51.

22. De Vos J, Devoogdt N, Lahoutte T, Muyldermans S. Camelid single-domain antibody-fragment engineering for (pre)clinical in vivo molecular imaging applications: adjusting the bullet to its target. *Expert Opin Biol Ther.* 2013;13:1149–1160.

23. Ackermann U, Yeoh SD, Sachinidis JI, Poniger SS, Scott AM, Tochon-Danguy HJ. A simplified protocol for the automated production of succinimidyl 4-[F-18] fluorobenzoate on an IBA Synthera module. *J Labelled Comp Radiopharm.* 2011;54:671–673.

24. Olafsen T, Sirk SJ, Olma S, Shen CKF, Wu AM. ImmunoPET using engineered antibody fragments: fluorine-18 labeled diabodies for same-day imaging. *Tumour Biol.* 2012;33:669–677.

25. Cai W, Olafsen T, Zhang X, et al. PET imaging of colorectal cancer in xenograft-bearing mice by use of an [18F]-labeled T84.66 anti-carcinoembryonic antigen diabody. *J Nucl Med.* 2007;48:304–310.

26. Di Gialleonardo V, Signore A, Glaudemans AWJM, Dierckx RAJO, De Vries EFJ. N-(4-[18F]-fluorobenzoyl)interleukin-2 for PET of human-activated T lymphocytes. *J Nucl Med.* 2012;53:679–686.

27. Lapi SE, Wahnishe H, Pham D, et al. Assessment of an [18F]-labeled phosphoramidate peptidomimetic as a new prostate-specific membrane antigen–targeted imaging agent for prostate cancer. *J Nucl Med.* 2009;50:2042–2048.

28. Zhang X, Cai W, Cao F, et al. [18F]-labeled bombesin analogs for targeting GRP receptor-expressing prostate cancer. *J Nucl Med.* 2006;47:492–501.

29. Johnström P, Clark JC, Pickard JD, Davenport AP. Automated synthesis of the generic peptide labelling agent N-succinimidyl 4-[18F]fluorobenzoate and application to [18F]-label the vasoactive transmitter urotensin-II as a ligand for positron emission tomography. *Nucl Med Biol.* 2008;35:725–731.

30. Wuest F, Köhler L, Berndt M, Pietzsch J. Systematic comparison of two novel, thiol-reactive groups for [18F]-labeling of peptide and proteins with the acylating agent N-succinimidyl-4-[18F]-fluorobenzoate ([18F]-SFB). *Amino Acids.* 2009;36:283–295.

31. Rosik D, Thibblin A, Antoni G, et al. Incorporation of a triglutamyl spacer improves the biodistribution of synthetic affibody molecules radiofluorinated at the N-terminus via oxime formation with [18F]-4-fluorobenzaldehyde. *Bioconjug Chem.* 2014;25:82–92.

32. Wu AM. Engineered antibodies for molecular imaging of cancer. *Methods.* 2014;65:139–147.